Heliyon 10 (2024) e30810

Contents lists available at ScienceDirect

Heliyon

journal homepage: www.cell.com/heliyon

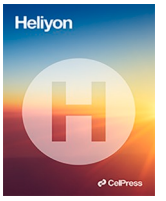

Research article

Extraction of gamma iron oxide (γ-Fe_2O_3) nanoparticles from waste can: Structure, morphology and magnetic properties

Bristy Biswas, Md. Lutfor Rahman *, Md. Farid Ahmed, Nahid Sharmin

Institute of Glass and Ceramic Research and Testing (IGCRT), Bangladesh Council of Scientific and Industrial Research (BCSIR), Dhanmondi, Dhaka, 1205, Bangladesh

ARTICLE INFO

Keywords:
Wasted iron cans
γ-Fe_2O_3
Acid leaching precipitation method
X-ray peak profiling
Saturation magnetization
Surface chemistry

ABSTRACT

In this work, the transformation of waste iron cans to gamma iron oxide (γ-Fe_2O_3) nanoparticles following acid leaching precipitation method along with their structural, surface chemistry, and magnetic properties was studied. Highly magnetic iron-based nanomaterials, maghemite with high saturation magnetization have been synthesized through an acid leaching technique by carefully tuning of pH and calcination temperature. The phase composition and crystal structure, surface morphology, surface chemistry, and surface composition of the synthesized γ-Fe_2O_3 nanoparticles were explored by X-ray diffraction (XRD), Scanning electron microscopy (SEM), X-ray photoelectron spectroscopy (XPS) and Energy-dispersive X-ray spectroscopy (EDS). The XRD results confirm the cubic spinel structure having crystallite size 26.90–52.15 nm. The XPS study reveals the presence of Fe, O element and the binding energy of Fe (710.31 and 724.48 eV) confirms the formation of γ-Fe_2O_3 as well. By dynamic light scattering (DLS) method and zeta potential analyzer, the particle size distribution and stability of the systems were investigated. The magnetic behavior of the synthesized γ-Fe_2O_3 nanoparticles were studied using a vibrating sample magnetometer (VSM) which confirmed the ferrimagnetic particles with saturation magnetization of 54.94 emu/g. The resultant maghemite nanoparticles will be used in photo-catalysts and humidity sensing. The net impact of the work stated here is based on the principle of converting waste into useful nanomaterials. Finally, it was concluded that our results can give insights into the design of the synthesis procedure from the precursor to the high-quality gamma iron oxide nanoparticles with high saturation magnetization for different potential applications which are inexpensive and very simple.

1. Introduction

Environment safety and climate change have been a prime focus area for the entire world recently. The disposal and recycling of environmental waste has become one of the biggest challenges of today's scientific research. To attain sustainable development through waste treatment and waste recycling, and value-added nanomaterial synthesis from waste materials is a very effective way that conforms to both the minimum waste generation and "Wealth from Waste" [1–3]. Among metals, a substantial amount of iron accumulates as waste condensed milk cans, beverage cans, coconut oil cans, mill scale, sludge, scrape, iron dust, slag, by-products of coke oven, refractory materials and sinter plant, as well as steel industries and so on. When these solid wastes are dumped in open

* Corresponding author.
E-mail addresses: lutforrahman@bcsir.gov.bd, lutforju33@yahoo.com (Md.L. Rahman).

https://doi.org/10.1016/j.heliyon.2024.e30810
Received 21 February 2024; Received in revised form 6 May 2024; Accepted 6 May 2024
Available online 9 May 2024

spaces and excavated land, environmental pollution is caused in the form of dust and leachate, at the same time huge financial liability is created due to the huge loss of valued materials and scarcity of land. In this work, waste condensed milk cans have been used as raw materials. These 'cans' are mainly made of iron. After using the inner materials, the cans are just thrown out drastically. So significant quantity of the said metal is wasted every year which can be used to produce useful magnetic materials by careful manipulation of synthetic conditions [4–8]. To address the facts the present study was designed to reuse these waste materials beneficially by converting them into a completely new valued product γ-Fe_2O_3 nanoparticles which can fulfill the need for a possible resource for meeting up increasing shortages of sustainable materials for photocatalysis and sensing.

The primary purpose of this invention is to recover metal values from iron-containing waste materials and convert them to magnetic γ-Fe_2O_3 nanoparticles having a wide range of applications from catalysis to waste management [9,10]. It is widely used for the production of, e.g., magnetic materials [11–13], sensing materials [14], pigments [15], sorbents [16,17], photocatalysts [16], storing data [18], for biomedical applications such as drug delivery [19,20], contrast agents for resonance imaging [21–23] and hyperthermia treatment [18,24], as well as being key components for adsorption and storage purposes [25,26]. Recently, iron oxides have been used in a huge amount as electrodes for sodium-ion, lithium-ion, and alkaline-ion batteries [27–31]. All these applications have different requirements regarding the thermal, chemical, mechanical, and magnetic properties of the particles, which are affected by the size, shape, and crystal structure of the nanomaterials [32–34].

The chemical formula of gamma iron oxide is γ-Fe_2O_3, in other words, maghemite, which is second in the most stable iron oxide polymorph. Because of its abundance, low cost, high chemical and physical stability, non-toxicity, and amazing magnetic characteristics, scientists and researchers are investigating maghemite widely. Maghemite is an n-type semiconductor with 2.0 eV band gap energy, thermally unstable, and ferrimagnetic in nature and transformed to hematite at higher temperatures. Hence, temperature below 450 °C is needed to produce γ-Fe_2O_3, which can be done by the dehydration of ferric hydroxides or oxidation of magnetite. All the iron cations in maghemite are in the trivalent state, and the charge neutrality is generated by the presence of the cation vacancies. With a cubic unit cell (a) 8.351 Å, maghemite possess the inverse spinel crystalline system; each of which contains $21\frac{1}{3}$ Fe^{3+} ions, $2\frac{1}{3}$ vacancies and 32 O^{2-} ions, Oxygen anions form a face -centered cubic (FCC) arrangement whereas the tetrahedral sites (eight Fe^{3+} ions per unit cell) and octahedral sites (comprising the remaining Fe^{3+} ions and vacancies) are occupied by the ferric ions. γ-Fe_2O_3 is easily magnetized which presents a high magnetic response when acquiesced to an external magnetic field [2,35].

Using a variety of techniques, maghemite nanoparticles have been made such as sol-gel [12], ball-milling [2], laser pyrolysis [36], solvothermal [37], microemulsion [37], sonochemistry, microemulsion using an ionic surfactant [2], sonochemical [2], and green synthesis routes [37,38] which are reported in the literature. Having a special emphasis on the studies of Mössbauer spectroscopy [39], Layek et al., 2011 reported an excellent review paper regarding the synthesis and properties of γ-Fe_2O_3 nanoparticles. However, in developing countries, recycling is not yet a favorable procedure where extraction of valued materials from metal wastage is very challenging and it will rescue precious metallic resources at the same time. For large-scale production, the instrumentation, machinery, and reagents cost are a big factor to look at. Herein, an acid leaching precipitation method for the production of γ-Fe_2O_3 nanoparticles from waste condensed milk can has been reported which is very simple. The extraction process was optimized through controlling pH and calcination temperature. The investigation of structural, morphological, surface chemistry and magnetic property were done using modern technique XRD, SEM, XPS and VSM. The main aim was to use waste cans to obtain potential gamma iron oxide nanomaterials thus adhering to the principle of generating "Wealth from Waste".

2. Methodology

2.1. Materials

For the synthesis of γ-Fe_2O_3 nanoparticles, the co-precipitation method was applied. The main raw material was discarded waste condensed milk cans of different brands collected from local tea stall areas of Bangladesh. Locally procured and analytical grade concentrated Hydrochloric acid (HCl) with 37 % assay (Merck Germany, 12.08 M), and Sodium Hydroxide pellets with ≥99 %, assay (Merck, Germany) were used without any purification. Laboratory-prepared Deionized (DI) water was employed in the experiment.

2.2. Preparation of γ-Fe_2O_3

To prepare γ-Fe_2O_3 nanoparticles from wasted condensed milk cans, firstly, iron chips were transformed into intermediate iron hydroxide from iron salt solution following an acid leaching technique which is the oxidation step and secondly, iron hydroxides were calcined at different temperatures to get γ-Fe_2O_3 nanoparticles. In the beginning, the collected cans were properly washed, cleaned, and burnt out to remove the organic layer by slow firing and then cut into small pieces for the highest leaching. A required amount of can chips was then taken in a beaker containing 1:1 HCl and subjected to heating until the chips were entirely gone into the solution. The temperature was set at 80°-90 °C and the time required to complete the leaching process was 1.50 h. Afterwards, the solution was allowed to reach at room temperature followed by filtration. The iron was precipitated by the dropwise addition of NaOH to the filtrate under magnetic stirring and the pH was varied to 12–14. By filtering the liquor, the precipitate was then collected and washed with DI water more than 10 times for the complete neutralization of the pH and removal of the unwanted ions like Cl-, Na+, etc. After that, the precipitate was desiccated at 110 °C for 24 h in the oven and the dried product was crushed and sintered at different temperatures (200–350 °C) for the change of iron hydroxide to maghemite for 3 h. The calcined brown products were crushed, and again washed several times to remove the impurities and soluble components. Finally, the washed powders were filtered and then dried at 110 °C for 3 h. The obtained gamma iron oxide was then again ground and stored. The synthesis procedure of γ-Fe_2O_3 nanoparticles is

represented in Fig. 1.

The rection mechanism of the synthesis procedure of γ-Fe_2O_3 nanoparticles from wasted iron can is given below:

$$Fe - chips + 2HCl \xrightarrow{80^\circ - 90^\circ C} FeCl_2 + \uparrow H_2$$

$$FeCl_2 + NaOH \rightarrow Fe(OH)_2 \downarrow + Fe(OH)_3 \downarrow + NaCl$$

$$Fe(OH)_2 + Fe(OH)_3 \xrightarrow{350^\circ C} \gamma - Fe_2O_3$$

2.3. Characterization

The raw material analysis of the collected samples was scrutinized by Wavelength Dispersive X-ray Fluorescence with the Model no. of Rigaku ZSX Primus IV. To determine the crystalline structure phase and phase of the synthesized gamma iron oxide particles, X-ray Diffractometer (Rigaku SmartLab SE, Japan) with a copper k-alpha source of 1.5406 Å (λ), 0.02° step size, 50°/min scan speed over a 2θ range (10°–80°), was used. Using Scanning Electron Microscopy (MA15 VP-SEM, Carl Zeiss Evo, UK), the morphology of γ-Fe_2O_3 nanoparticles was carried out and the average particle sizes of the prepared samples were calculated by ImageJ software from the respective SEM images. The Energy Dispersive X-Ray Spectrometer, EDS (EDAX team, EDAX, USA) explored the chemical composition of the product. To evaluate the chemical and oxidation state of the atoms in the synthesized γ-Fe_2O_3 nanoparticles, an X-ray photoelectron spectrometer (K-alpha, Thermo Scientific, Czech Republic) was used with a monochromatic X-ray source of Al K-alpha (1486.69 eV). With 400 μm^2 spot size area, 200 eV pass energy, 5 scans, and 1.0 eV energy step size, the survey scan analyses of the samples were carried out. To obtain Fe 2p spectra, the high-resolution scan analyses of the samples were performed where the pass energy for the high-resolution was 50 eV, 15 scans, and 0.10 eV energy step size. The particle size distribution of the product was also been observed by dynamic light scattering based Nanoparticle Analyzer (nanoPartica SZ-100-S2, HORIBA scientific Ltd, Japan) in the liquid environment. A few microliters of diluted material were dropped into the cell and examined by DLS. Using the technique of Laser Doppler Velocimetry (LDV), a Zetasizer (Zetasizer Ultra, ZSU5700, Malvern, UK) measured the Zeta potentials of gamma iron oxide nanomaterials. The Vibrating Sample Magnetometer (VSM, Model: EV VSM System, Brand: Microsense, USA) investigated the magnetic property of calcined γ-Fe_2O_3 particles at room temperature with a maximum field of ±10 kOe.

3. Results and discussion

3.1. Raw material analysis

The main chemical composition of the collected waste condensed milk cans of different brands (Brand S1, Brand S2 and Brand S3) are given in Table 1. All the cans contain above 97 % of iron. Other elements like Na, Ca, Cu, S, Al, Mg, Cr, K etc. are present in minutes amount. So, the waste cans will be a suitable iron source to extract valued materials.

3.2. Process optimization

Generally, the target of process optimization is to get maximum percent yield of the products having high phase purity, and better properties. In the current research, effects of different process parameters on the extent of yield were studied to optimize the synthesis process of gamma iron oxide. Two sets of experiments were conducted to get higher yield with better magnetic properties of the

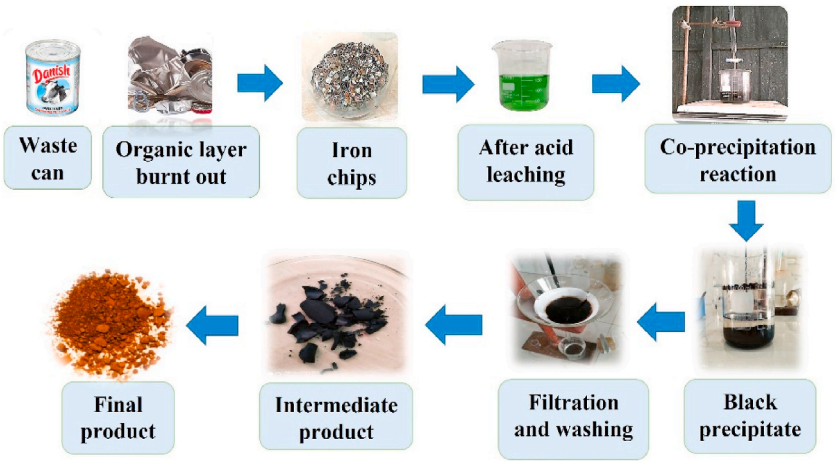

Fig. 1. Schematic diagram for preparation of γ-Fe_2O_3 nanoparticles.

Table 1
Raw material analysis report.

Component	Content (wt. %)		
	Brand S1 (%)	Brand S2 (%)	Brand S3 (%)
Fe	99.4	99.1	97.5
Mn	0.268	0.217	0.170
Sn	0.0306	0.221	2.08

synthesized γ-Fe_2O_3, while changing the value of one parameter, either pH or calcination temperature at a time, keeping another fixed. Impurity formation was avoided as minimum as possible.

3.2.1. *Effect of pH*

From Fig. 2a, the effect of pH on the percent yield and magnetic properties of gamma iron oxide particles can be seen. The pH of the solution was adjusted between 12, 13 and 14 for the precipitations of iron as iron hydroxides, three experiments were carried out by varying the amount of NaOH solution with stirring and keeping the other parameter constant. It was found that the percent-yield increases from 90.91 % to 97.02 % with the increase of pH from 12 to 14. This can be attributed by the increased amount of iron hydroxide precipitate with the increase of pH which in turn increased the yield of the product. At pH 14, the highest percentage of yield was formed. So, the magnetic properties of gamma iron oxide are greatly influenced by pH, which was proved by the values obtained from VSM that showed highest magnetization at pH 14.

3.2.2. *Effect of calcination temperature*

Fig. 2b represents the calcination temperature effect on the product yield of gamma iron oxide as well as the magnetic properties. Four experiments varying calcination temperatures at 200 °C, 250 °C, 300 °C and 350 °C were carried out for 3 h to convert iron hydroxide to gamma iron oxide nanoparticles (GIONPs), maintaining other condition at optimum level. From Fig. 2b, it is clear that the percent yield is decreasing with the increase of temperature for all synthesized γ-Fe_2O_3 nanoparticles. The reason behind this may be ascribed to the formation of some iron (III) oxide-hydroxide (FeOOH) instead of ferric oxide (γ-Fe_2O_3). With the increase in temperature, FeOOH formation became lower, and all iron hydroxides were transformed into γ-Fe_2O_3, exhibiting the strongest magnetic property at its ideal temperature of 350 °C.

3.3. *X-ray diffraction (XRD) analysis*

The phase composition and the crystal structure of the synthesized products studied by X-ray Diffractometer are represented in Fig. 3. In the XRD diffractogram, the characteristic peaks of the samples at 2θ = 14.92°, 30.13°, 35.50°, 43.25°, 53.56°, 57.14° and 62.73° corresponding to the (1 1 0), (2 2 0), (3 1 1), (4 0 0), (4 2 2), (5 1 1) and (4 4 0) planes are very well matched with the standard 2θ values of maghemite according to JCPDS Card no. 00-039-1346 which confirms the formation γ-Fe_2O_3 phase. The prepared γ-Fe_2O_3 particles have a cubic spinel crystal system, with the independent lattice parameters a = b = c = 8.351. The sharp characteristic peaks of the XRD patterns indicate the fully crystallized γ-Fe_2O_3 nanoparticles. In the case of sample S6, γ-Fe_2O_3 particles synthesized at T350 °C and pH 14, no impurity phase was detected in the XRD pattern whereas samples S5 and S4, synthesized at T350 °C, with pH 13 and pH 12, comprised of some small quantities of impurities (generally hematite - JCPDS card no. 01–080-237 and iron (II) oxide-ICDD card no. 01–078-6916) (Fig. 3) [40,38].

With the rising of calcination temperatures, crystallite sizes are increasing and the width of the prominent peaks are growing sharper whereas crystallite sizes are decreasing with the increase of pH as shown in Fig. 3. In the case of S5 (pH 13) and S6 (pH 14) with calcination temperature 350 °C, the peak is broadening means crystallite size is decreasing. According to crystallization theory, if the solubility limit of the species is decreased, supersaturation is introduced to the system which will determine the rate of nucleation. For smaller crystals, the degree of supersaturation has to be higher favoring nucleation and a greater number of smaller crystals may be produced and vice-versa for bigger crystals. Fewer nuclei will favor particle growth. Sazaki et al. (1994) reported that the number of crystals initially decreases and then increases with increasing supersaturation [38,41]. So, pH and temperature have a great effect on crystal size.

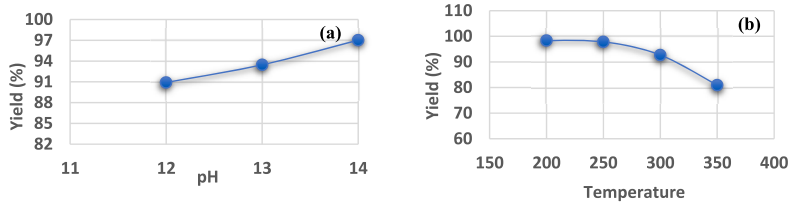

Fig. 2. Effect of (a) pH and (b) calcination temperature on the yield of γ-Fe_2O_3.

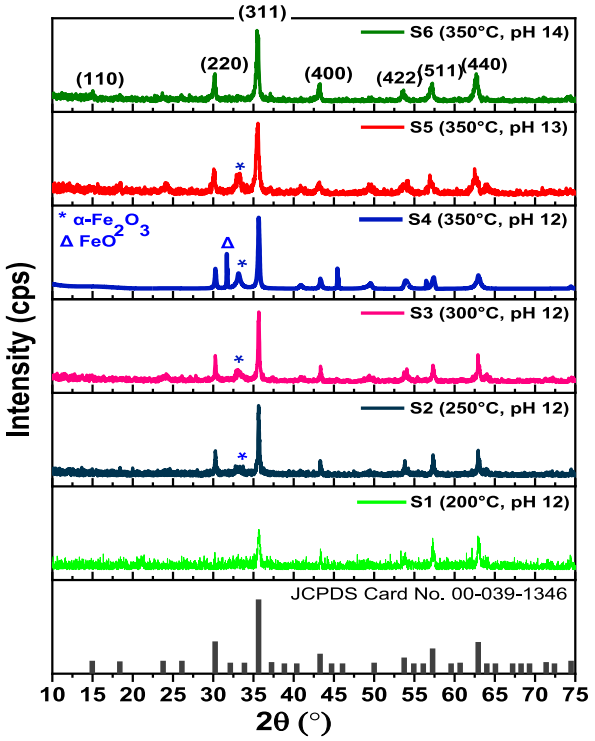

Fig. 3. X-ray diffraction pattern of γ-Fe_2O_3 nano particles of different pHs and CTs.

3.3.1. *Debye-Scherrer method and Wilson method*

Among different methods for determining the size of crystallite size by peak broadening analysis technique, Debye-Scherrer method is the simplest technique for calculating the average crystallite size (D) where the full width at the half maximum (FWHM) value of the highest peak is used in Eq. (1) [41,42].

$$D_{D-S} = \frac{K\lambda}{\beta_D \cos\theta} \tag{1}$$

where, $D_{D\text{-}S}$ is the crystallite size (nm), K is the shape factor (0.9), λ is the wavelength of XRY (0.154060 nm), θ is the diffraction angle and β_D is the internal breadth (in radians). Lattice strain is the result of crystal defects, distortion and lattice mismatch in powder sample which can be expressed by Stokes and Wilson equation **eqn. (2)** [42,43]

$$\varepsilon = \frac{\beta_{strain}}{4\ tan\ \theta} \tag{2}$$

where, ε is the lattice strain and β_{strain} is the integral breadth for strain effect [44]. The calculated crystallite sizes ($D_{D\text{-}S}$) and strain are tabulated in Table 2.

3.3.2. *Williamson–Hall method*

Williamson and Hall method is one of the easiest integral breadth techniques where size induced and strain induced peak broadening are differentiated by studying the peak breadth as a function of 2θ [45]. The peak broadening resulted from the lattice

Table 2
Crystallite size and lattice strain of the γ-Fe_2O_3 nanoparticles by Debye-Scherrer and Williamson-Hall plot.

Sample ID	Debye-Scherrer method and Wilson method		Williamson–Hall method	
	$D_{D\text{-}S}$ (nm)	Strain $\varepsilon_W \times 10^{-4}$	$D_{W\text{-}H}$ (nm)	Strain $\varepsilon_{W\text{-}H} \times 10^{-3}$
S1 (200 °C, pH 12)	43.92	2.67	72.98	2.37
S2 (250 °C, pH 12)	46.35	2.52	90.62	2.31
S3 (300 °C, pH 12)	49.08	2.38	101.95	1.67
S4 (350 °C, pH 12)	52.15	2.24	119.53	1.55
S5 (350 °C, pH 13)	27.80	4.19	59.51	3.12
S6 (350 °C, pH 14)	26.90	4.33	58.26	3.24

strain is represented by the Stokes and Wilson formula [41,46].

$$\beta_{strain} = 4\varepsilon \tan\theta \tag{3}$$

The breadth of the observed line is found by the addition of the β_{strain} and β_D, after subtracting the instrumental broadening.

$$\beta_{hkl} = \beta_{strain} + \beta_D \tag{4}$$

Here, β_{hkl} is FWHM of a radiant peak, β_{strain} and β_D are the width occurred from strain and size. Putting the value of β_{strain} and β_D from equations (1) and (3), we get

$$\beta_{hkl} = 4\varepsilon \tan\theta + k\lambda/D\cos\theta \tag{5}$$

by rearranging equation (4),

$$\beta_{hkl}\cos\theta = 4\varepsilon \sin\theta + k\lambda/D_{W-H} \tag{6}$$

The above equations (4) and (5) are Williamson-Hall equations. Equation (6) looks like the straight-line equation, y = mx + c. By plotting the value of 4sinθ along the x-axis and the value of $\beta_{hkl}\cos\theta$ along the y axis [47], W–H plot is drawn for the 6 samples as shown in Fig. 4 (S1 – S6). From the linear fit to the data, the crystallite size has been estimated from the y-intercept, and the strain has been obtained from the slope of the straight line. The estimated values of crystallite size ($D_{W\text{-}H}$) and lattice strain ($\varepsilon_{W\text{-}H}$) are recorded in Table 2.

3.3.3. Different microstructural parameters determination

In a crystalline material, the length of dislocation lines in a unit volume is known as dislocation density (δ) which can be expressed by Williamson and Smallman's formula from the following **eqn. (7)** [43]:

$$\delta = \frac{1}{D^2} \tag{7}$$

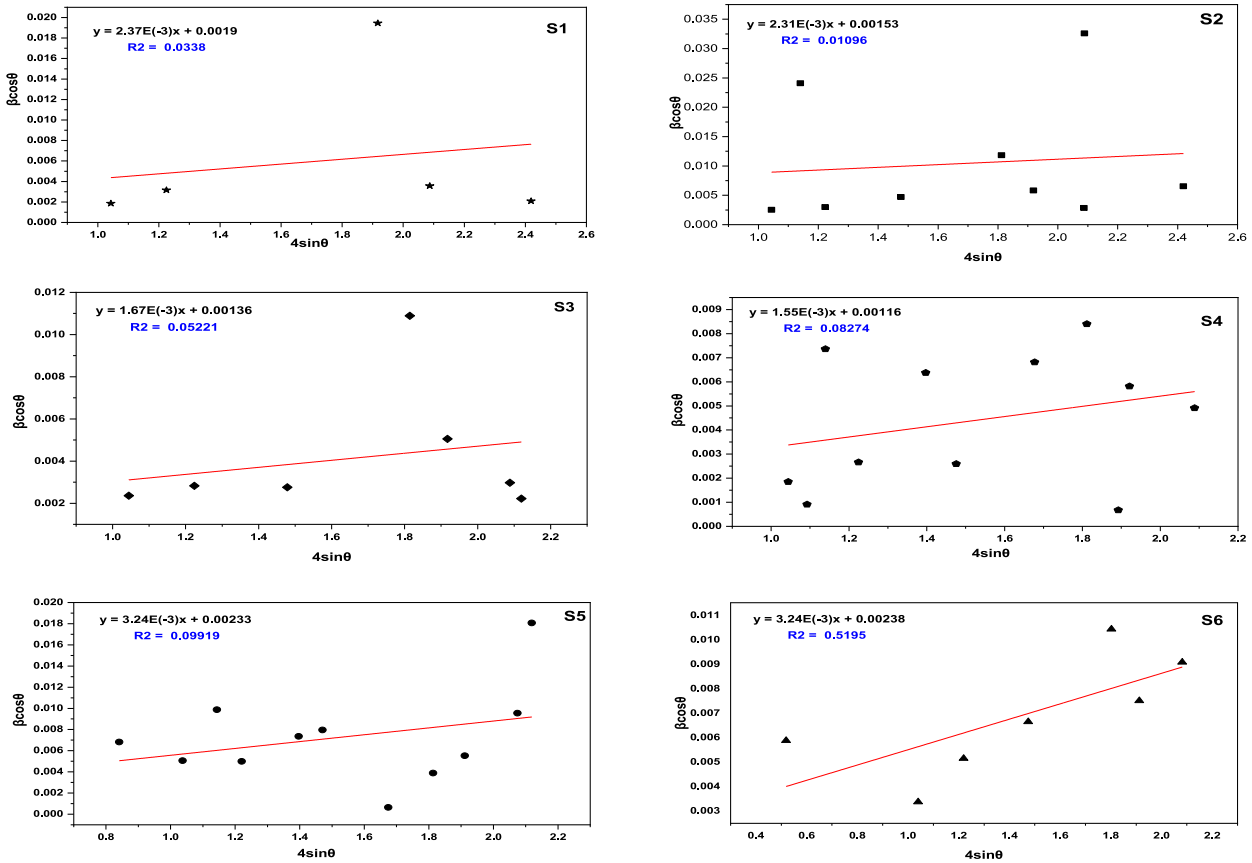

Fig. 4. W–H plot of synthesized S1, S2, S3, S4, S5 and S6 γ-Fe_2O_3 nanoparticles.

where "D" is the crystallite size.

The lattice constants of the nanoparticles have been calculated from the subsequent calculations from **eqns. (8) and (9)** [45]. Here "d" is the interplanar spacing and "n" is the order of diffraction which is generally equal to 1 [41].

$$2dsin\theta = n\lambda \tag{8}$$

$$a = d\sqrt{h^2 + k^2 + l^2} \tag{9}$$

where, "a" is represented as the lattice constant and the integers h, k and l are Miller indices of diffraction planes. The cube of the lattice constant "a" is equal to the cell volume [45] which is expressed in Eq. (10). Table 3 records different microstructural parameters of the synthesized γ-Fe_2O_3 nanoparticles on the basis on different pH and calcination temperature.

$$V = a^3 \tag{10}$$

From the above Tables 2 and 3 and it is observed that the value of δ, ε, a and V primarily decrease as a consequence of rising D value as well as temperature and then increase with decreasing crystallite size and rising pH of the solution [44].

3.4. Morphological analysis by SEM

Scanning Electron Microscopy investigation was used to explore the surface morphology of γ-Fe_2O_3 nanoparticles. Fig. 5 (S1 – S6) shows the morphology and particle size distribution (PSD) histograms of the prepared γ-Fe_2O_3 particles from waste condensed milk cans at distinct calcination temperatures and pH. As represented in Fig. 5 (S1 – S6), uneven round-shaped particles are found with some agglomerations.

A higher ratio of surface area to volume is the reason of the resulting accumulation producing numerous crystals to combine together forming bigger particles and also for the grain growth at higher calcination temperature for the contraction of Gibbs free energy producing from the reduction of the extended surface area of nanoparticles [48–50]. The mean particle sizes of the synthesized samples are increasing with increasing calcination temperatures and decreasing with the increase of pHs due to gain growth and electrostatic repulsion respectively [51,52].

Using Image J software, the average particle sizes have been calculated which are larger than the crystallite sizes obtained from the XRD data and are recorded in Table 4. The range of particle size distribution is 92 nm–126 nm. The lowest particle size is 92 nm for sample S1, while the highest one is 157 nm for sample S4.

3.5. Particle size analysis

The results of particle size distribution in the solution form at 25 °C observed by DLS-based Nanoparticle Analyzer are represented in Fig. 6.

It is clearly observed from Table 5 that the prepared γ-Fe_2O_3 nanoparticles are poly dispersed with a narrow particle size distribution having PDI (Polydispersity Index) value 0.509 to 0.612. The cumulative mean particle size of the prepared γ-Fe_2O_3 nanoparticles has increased with increasing calcination temperatures which are in the range from 315.27 nm to 837.07 nm (Table 5). According to DLS theory, When the particles are dispersed in a solvent or a medium, an electrical double layer adhere to the surface of the particles which means that DLS based particle size gives the size of the core particle, coating and solvent layer attached to the particles. On the other hand, SEM gives the information of core particles only. As a result, the hydrodynamic diameter obtained from Nanoparticle Analyzer is always bigger from the desiccated diameter from SEM micrographs [47,53,54] and the particle size increases following the same pattern like the SEM result [55].

3.6. Compositional analysis

Energy Dispersive X-ray Spectroscopy (EDS) was used to determine the existence of constituents and their atomic weight percentage in the γ-Fe_2O_3 nanoparticles, as represented in Fig. 7 (S1 – S6).

The purity and presence of Fe and O atoms in the synthesized γ-Fe_2O_3 nanoparticles with good elemental percentages are exhibited from the EDS spectrum as recorded in Table 6. From the EDS spectra, it is clear that only one oxygen (O) peak and three iron (Fe) peaks

Table 3
Effect of temperature and pH on various microstructural parameters.

Sample ID	Dislocation density, $\delta \times 10^{14}$ (lines/m^2)		Lattice constant (Å)	Cell Volume (Å^3)
	D-S method	W–H method		
S1 (200 °C, pH 12)	5.18	1.91	8.3483	581.82
S2 (250 °C, pH 12)	4.65	1.55	8.3469	581.55
S3 (300 °C, pH 12)	4.15	1.09	8.3466	581.48
S4 (350 °C, pH 12)	3.67	0.81	8.3460	581.34
S5 (350 °C, pH 13)	12.9	2.77	8.3463	581.41
S6 (350 °C, pH 14)	13.8	3.07	8.3463	581.41

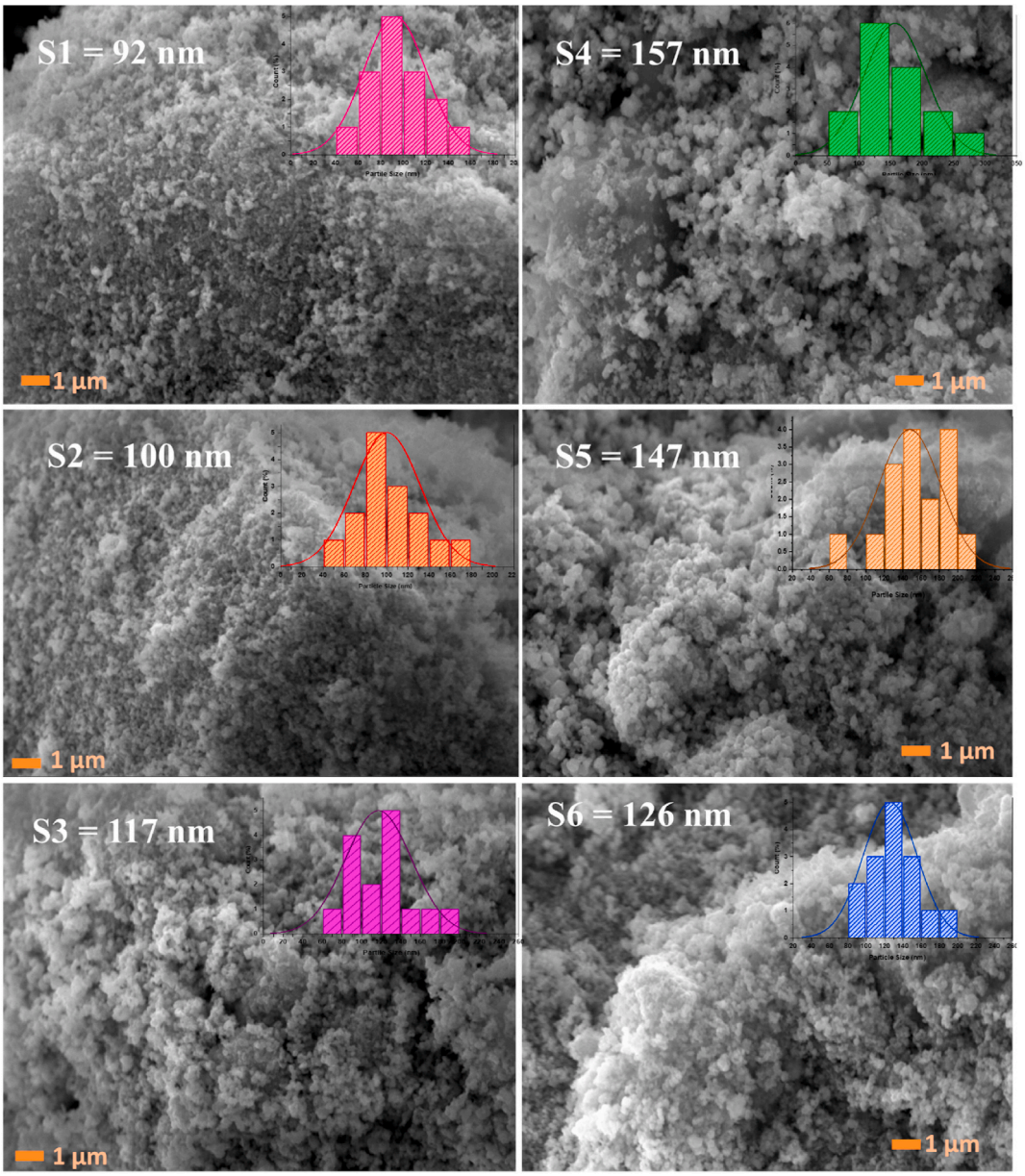

Fig. 5. SEM micrographs and size distribution of S1, S2, S3, S4, S5 and S6 samples.

Table 4
Average particle sizes of γ-Fe_2O_3 nanoparticles.

Sample ID	Average Particle Size (nm)
S1 (200 °C, pH 12)	92
S2 (250 °C, pH 12)	100
S3 (300 °C, pH 12)	117
S4 (350 °C, pH 12)	157
S5 (350 °C, pH 13)	147
S6 (350 °C, pH 14)	126

are found in all the prepared maghemite particles. No peak was observed rather than the expected Fe and O, for samples S1, S2, S4, S5, and S6 which identify that the synthesized product is highly pure. Whereas two additional signals for Na and Cl were observed in the sample S3 calcined at 300 °C. The atomic ratio of Iron and Oxygen was around the stoichiometric value of 0.66 for all the samples.

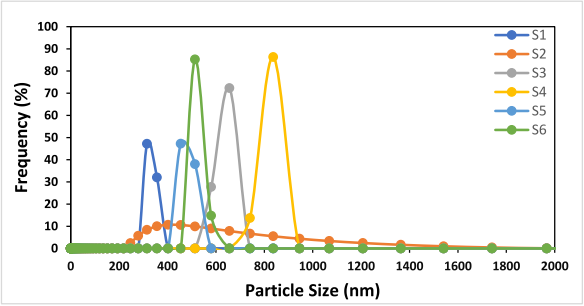

Fig. 6. Nanoparticle size distribution of S1, S2, S3, S4, S5 and S6 samples.

Table 5
Particle size distribution results of synthesized γ-Fe_2O_3 nanoparticles.

Sample ID	Average Particle Size (nm)
S1 (200 °C, pH 12)	315.27
S2 (250 °C, pH 12)	402.44
S3 (300 °C, pH 12)	655.76
S4 (350 °C, pH 12)	837.07
S5 (350 °C, pH 13)	513.71
S6 (350 °C, pH 14)	454.69

3.7. Zeta potential

The stability of γ-Fe_2O_3 nanoparticles dispersed in liquid medium was investigated by measuring the zeta (ζ) potential and results are shown in Fig. 8 (S1 – S6). To measure zeta potential value of γ-Fe_2O_3 nanoparticles, 10 mg of each sample were mixed with 100 ml deionized water and then sonicated for 30 min using ultrasonic homogenizer (model: LUH 105, brand: Labocon, UK). After that, the dispersed solutions were treated in neutral (pH~7) [56,57]. Thus, the solution was prepared for zeta potential measurement.

The Zeta potential of the prepared samples was measured by the Nanoparticle Analyzer and recorded in Table 7. The difference of potential among the sliding plane in the electronic double layer and the bulk potential is called Zeta potential. While colloidal stability is linked to steric and electrostatic repulsion, measurements of zeta potential generally give a good indication representing the degree of electrostatic repulsion among the nanoparticles as zeta potential is associated to the surface charge on nanoparticles. The zeta potential with an absolute value higher than ±30 mV, is typically assumed as electrostatically stable particles [58–60]. Here sample S6 has achieved the highest zeta potential value which is +47.9 mV. The second, third and fourth highest zeta potential values are achieved for the samples S3, S1 and S4 which are +34.7 mV, +33.2 mV and +31.9 mV. But the sample S2, and S5 have a potential value of +20.6 mV, and −0.8 mV which are lower than the absolute value of ±30 mV. So, S6, S3, S1, and S4 are stable in dispersion but, S2, and S5 are unstable in dispersion. The reason for lower zeta potential value can be ascribed by Ohshima's model where high zeta potential value is attributed for tiny particles and lower for particles with bigger size due to the intense thickness of opposite charged ion of small particles than bigger particles [47,50].

When the repulsion surpasses the attraction, then a steady system is formed [61]. Particles with a large positive or negative zeta potential value have a strong tendency to repel each other and there is zero tendency for the particles to come together. In DLVO theory, a system is considered as stable, when the van der Waals attractive force is dominated by the electrostatic repulsive force [62].

3.8. Magnetic properties analysis

The room temperature (300K) magnetic hysteresis loops (M − H) of prepared γ-Fe_2O_3 nanoparticles are presented in Fig. 9 which describe the dependence of magnetism on the applied magnetic field upon the basis of microstructure and chemical phase of nanoparticles as non-crystalline sample possess zero magnetism [35]. Table 8 represents the magnetic property like magnetic saturation (Ms), coercive field (Hc), residual magnetization (Mr), and squareness ratio (Mr/Ms) achieved from hysteresis loops measurement.

All the prepared γ-Fe_2O_3 nanoparticles synthesized at different temperatures and pH exhibited good magnetic properties at room temperature indicating a moderate degree of ordering in Fe^{3+} cation vacancy in the as prepared γ-Fe_2O_3 nanoparticles [63]. In Fig. 9 the M − H loops showed characteristic S-shaped curves of ferrimagnetic materials. From the Hc value range from 49.01 Oe to 65.45 Oe and the Mr value range from 0.23 Oe to 4.26 Oe, it is proved that gamma ferric oxide is a soft ferrite in nature.

All six samples possess hysteresis loops with magnetic saturation (Ms), residual magnetization (Mr) and coercive force (Hc), which have been affected by the size and shape of the synthesized particles. The measurement of magnetic parameters at room temperature reveals that the coercive force decreases first and then rises with increasing calcination temperature at the same pH and after 300 °C, Hc again increases whereas the magnetization continuously increases and retentivity decreases with increasing calcination temperature and pH as well.

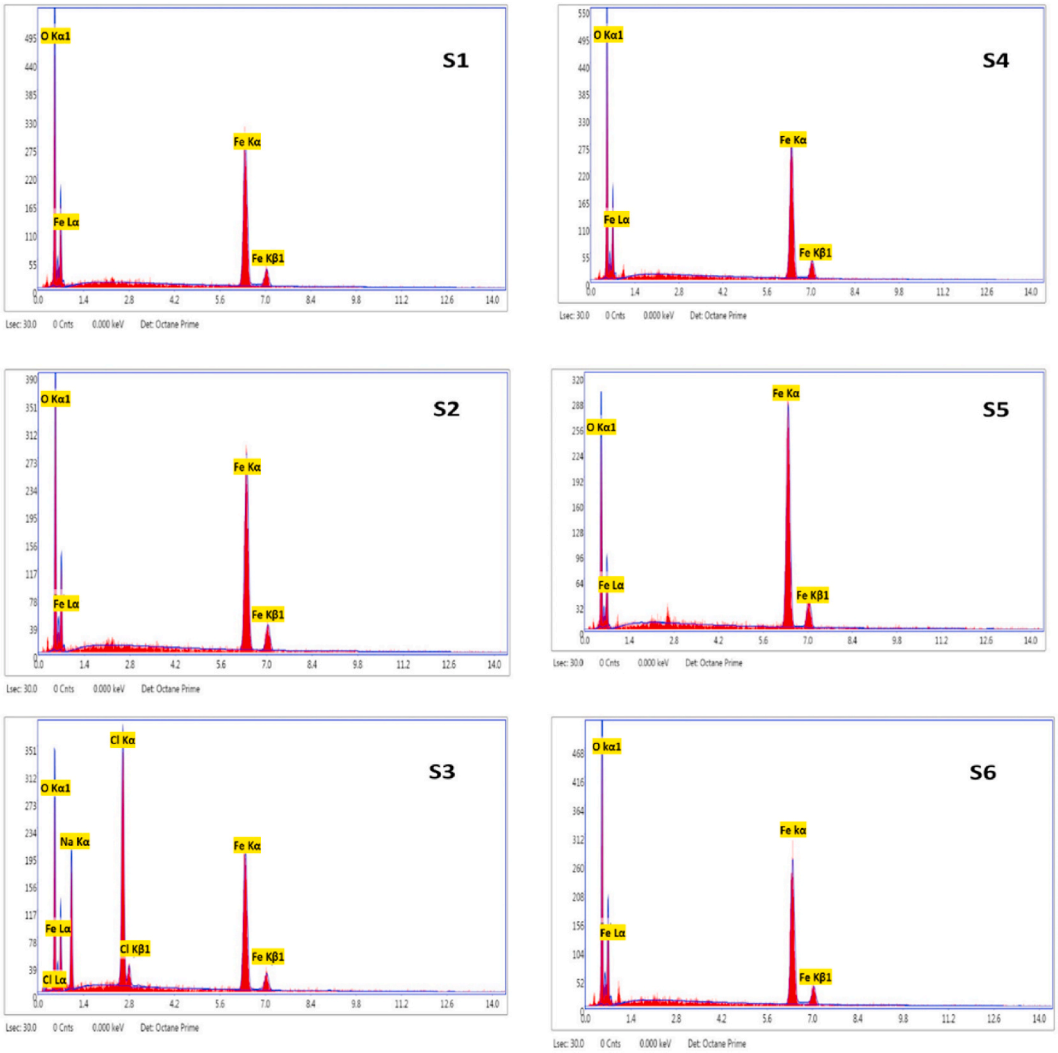

Fig. 7. EDS spectra of γ-Fe_2O_3 nanoparticles.

Table 6
Atomic percent of γ-Fe_2O_3 nanoparticles at different calcination temperature and pH.

Sample ID	Atomic %		Ratio
	Fe	O	Fe/O
S1	38.84	61.16	0.64
S2	42.72	57.28	0.74
S3	19.92	42.12	0.47
S4	37.55	62.45	0.60
S5	41.23	58.77	0.70
S6	38.26	61.74	0.62

In terms of the calcination temperature effect, the nano-particles emerge into strong magnetism immediately when γ-Fe_2O_3 is appeared at 200 °C (S1), having the lowest value of saturation magnetization (Ms) of about 31.98 emu/g which is supported by the XRD data of incomplete γ-Fe_2O_3 phase. With increasing CT, the Ms value also increases gradually. The higher values of Ms are observed with increasing pH. This is because, higher pH favors the formation of precipitation of metallic ions. At pH 12, the Ms is 32.60 (S4) whereas it is 39.71 at pH 13 (S5). When calcination temperature reaches 350 °C having the highest pH value of 14 (S6), Ms reached to the highest saturated magnetization, 54.94 emu/g, similar to bulk γ-Fe_2O_3 particles (Ms = 60–80 emu/g) [32,47,43,64] owning to the better nanocrystalline particle, consistent with both the XRD data and SEM result [65,66]. Saturation magnetization is low for samples calcined at low temperatures and pH, because of the presence of non-magnetic phase. Stokes and Wilson also suggests that higher

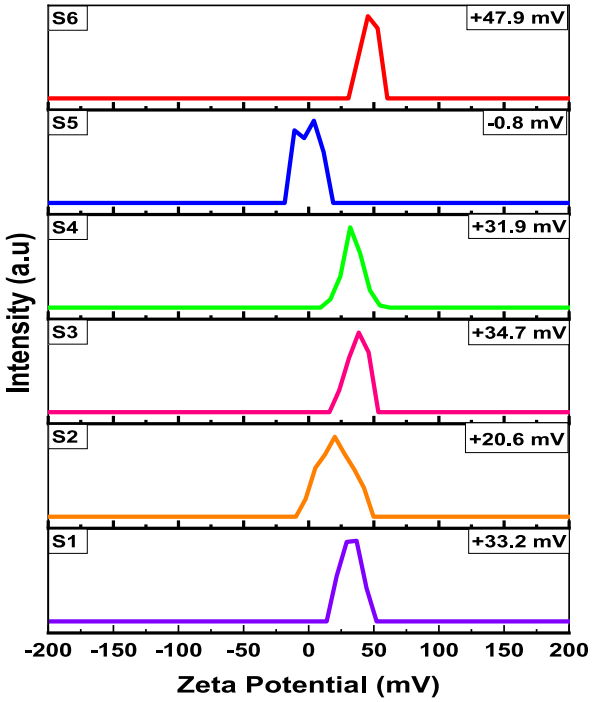

Fig. 8. Zeta potentials results of prepared S1, S2, S3, S4, S5 and S6 γ-Fe_2O_3 nanoparticles.

Table 7
Zeta potential results of γ-Fe_2O_3 particles.

Sample ID	Zeta potential (mV)
S1 (200 °C, pH 12)	+33.2
S2 (250 °C, pH 12)	+20.6
S3 (300 °C, pH 12)	+25.7
S4 (350 °C, pH 12)	+31.9
S5 (350 °C, pH 13)	−0.8
S6 (350 °C, pH 14)	+47.9

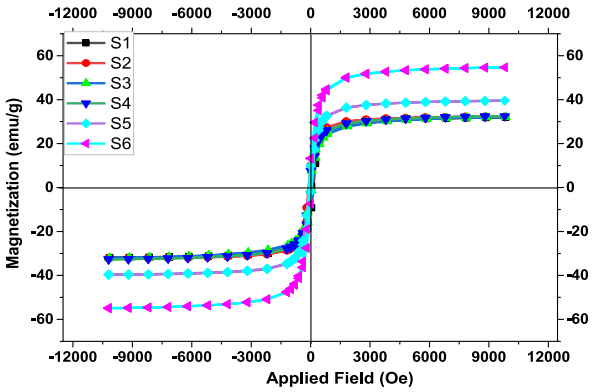

Fig. 9. M − H loop of γ-Fe_2O_3 particles Synthesized by Co-precipitation.

crystallinity is beneficial to enhanced Ms value of the sample [44].

Magnetic anisotropy (K), which prevents the magnetic momentum from aligning in an applied field is reduced first and increased leading to an increase in coercivity and saturation magnetization. The values of magnetic anisotropy can be calculated by Eq. (11) [50, 67,68].

Table 8
Saturation Magnetization (Ms), Coercivity (Hc), Remanent magnetization (Mr), Magnetic anisotropy (k) and Squareness Ratio and Magnetic Moment (ηB) of synthesized γ-Fe_2O_3 nanoparticles.

Sample ID	Ms (emu/g)	Hc (Oe)	Mr (Oe)	K	Mr/Ms	*(ηB)*
S1 (200 °C, pH 12)	31.98	53.25	4.26	1773.89	0.133	0.914
S2 (250 °C, pH 12)	32.30	49.92	3.12	1679.60	0.097	0.923
S3 (300 °C, pH 12)	32.32	49.01	3.04	1650.00	0.094	0.924
S4 (350 °C, pH 12)	32.60	54.44	2.09	1848.69	0.064	0.932
S5 (350 °C, pH 13)	39.71	62.22	1.47	2573.70	0.037	1.135
S6 (350 °C, pH 14)	54.94	65.45	0.23	3745.65	0.004	1.571

$$K = \frac{M_s \times H_c}{0.96} \tag{11}$$

with increasing calcination temperature and pH an increase in magnetic saturation *(M_s)* and moment *(η_B)* are noticed (Table 7), which is due to the ordering of Fe^{3+} cation vacancy. The magnetic moment *(η_B)* can be assessed from Eq. (12) [68].

$$\eta_B = \frac{MW \times M_s}{5585} \tag{12}$$

At pH 14 and 350 °C temperature, the magnetic saturation value of γ-Fe_2O_3 nanoparticles particles was the highest whereas the opposite action was noticed for the squareness ratio as well. The squareness ratio or remanence ratio is less than 0.5 for all γ-Fe_2O_3 nanoparticles (Table 8), suggesting that the synthesized γ-Fe_2O_3 nanoparticles have small single domain with a random direction and interact by magneto-static interactions.

A detailed comparison of the extracted γ-Fe_2O_3 nanoparticles of the current research has been carried out with the existing literature which include the precursor materials, synthesis methods, microstructural parameters, magnetic properties as well as its probable applications to understand the impacts of current research (Table 9).

3.9. XPS study

To explore the surface chemistry of the synthesized γ-Fe_2O_3 nanoparticles which is opposite to Fe_3O_4, X-ray photoelectron spectroscopy (XPS) analysis of prepared γ-Fe_2O_3 samples is carried out in addition, as presented in Fig. 10 [35]. Fig. 10a shows the high-resolution XPS survey spectrum data of the synthesized γ-Fe_2O_3 nanoparticles at 14 pH and 350 °C sintering temperature, whereas Fig. 10b displays the narrow scan for Fe 2p spectra. It was already revealed that iron (Fe) and oxygen (O) were the primary composition of γ-Fe_2O_3 particles. Apart from Fe 2p, O 1s, and the C 1s peaks in the spectrum, there are trace amount of Na coexisting and the C element of binding energy 284.8 eV ascribed to the contaminated carbon from air absorbed on the sample surface (Fig. 10).

In particular, Fe $2p_{3/2}$ spectra (Fig. 10b) exhibit two peaks at 710.31 and 724.48 eV, which are the characteristic peaks of the 3+ ion of γ-Fe_2O_3 [75,76] and there is no signal or shoulder at smaller binding energies as would be expected for the presence of the Fe^{2+} ion (~708 eV) [77]. Generally, Fe 2p XPS analysis shows broad peak of Fe^{3+} compared to Fe^{2+} and a satellite peak of Fe^{3+} is observed at approximately 8.0 eV higher than Fe $2p_{3/2}$ peak, whereas a satellite peak of Fe^{2+} is located at about 5.0–6.0 eV above Fe $2p_{3/2}$ peak [78]. Moreover, an additional peak, refereeing as the shakeup satellite peak at about 718.7 eV proves the absence of the Fe^{2+} ion in the prepared γ-Fe_2O_3 nanoparticles. The results of XPS spectra are consistent with the finding of XRD diffractogram patterns.

The peak in the narrow scan for oxygen (Fig. 10c) at the binding energy 529.7 eV was attributed for lattice Fe^{3+}-O bonded oxygen and 531.4 eV for oxygen bonded with moisture molecule associated on the surface of the γ-Fe_2O_3 nanoparticles by physisorption process [79]. The FWHM of the peak 2.84 eV suggest the chemisorption phenomena in the sample [80]. So, the interaction of moisture with the synthesized γ-Fe_2O_3 nanoparticles following chemisorption and physisorption methods recommend the suitability as humidity sensor.

4. Conclusion

The magnetic γ-Fe_2O_3 nanoparticles have been successfully synthesized from 'wasted iron cans' by a simplistic, low-cost acid leaching precipitation method. The synthesis process was optimized through variation of calcination temperature and pH. The X-ray crystallographic data were used to calculate the crystal size, strain, lattice constant, cell volume and dislocation density using Debye-Scherrer and Williamson-Hall method. In both cases, increased crystallite sizes, lattice strain and decreased dislocation density, lattice constant, cell volume were found with increasing calcination temperatures, which was completely in opposite manner for pH. As expected, the average particle sizes obtained from SEM were bigger than the crystallite sizes but smaller than the particle sizes from the DLS-based Nanoparticle Analyzer. More importantly, the composition of the gamma iron oxide nanomaterials was tuned with variations of the synthesis conditions. The results obtained from different characterization recommend that sample S6 (350 °C and pH 14) was the optimal product with 26.90 nm crystallite size, 8.3463 Å lattice constant, 126 nm and 454.69 nm particle sizes from SEM and DLS as well as +47.9 mV zeta potential. The high-resolution XPS survey spectrum data of γ-Fe_2O_3 nanoparticles revealed that the synthesized nanoparticles were predominately made up of iron (Fe) and oxygen (O) and exhibited the distinctive peaks of the Fe^{3+} ion associated with γ-Fe_2O_3. The room temperature magnetic measurements of the synthesized γ-Fe_2O_3 nanoparticles exhibit the

Table 9
Comparison of the current research with the literature.

Precursor	Synthesis procedure	Final Product	Crystallite size (nm)	*Ms (emu/g)*	*Hc (Oe)*	Application	Ref.
Scrap iron	Hydrothermal	γ-Fe_2O_3 nanoparticles	20 to 40	0.3813	10	Environmental waste management	[1]
Iron pentacarbonyl, $Fe(CO)_5$	Microwave plasma synthesis	γ-Fe_2O_3 nanoparticles	2 to ~50	13.2–67.6	–	Impact of size reduction	[7]
Slag, mill scale, scrap and iron dust	Co-precipitation	γ-Fe_2O_3 particles	11.04 to 18.62	17.44–41.69	3.464–60.193	Waste disposal problem	[42]
Waste Toner Powder	Thermal transformation technique	Magnetic iron oxide nanoparticles	32.07	19.5	–	Preparation of Recyclable Co(II)–NH_2–SiO_2@Fe_2O_3	[69]
Iron chloride and urea	Co-precipitation	γ-Fe_2O_3 nanoparticles	60	0.025	1250	Removal of toxic heavy metals from electroplating wastewater	[70]
Recyclable electro-coagulated sludge	Electrocoagulation method	γ-Fe_2O_3 nanoparticles	28.3	–	–	Wastewater treatment	[71]
Rusty iron nails from scrap metal	Electrochemical method	γ-Fe_2O_3 nanoparticles	7.54	–	–	Purification of Industrial Waste Water	[72]
Waste green vitriol	Solid-phase reduction-oxidation reaction	γ-Fe_2O_3 nanoparticles	35	–	–	adsorption of arsenite	[73]
Iron (III) acetylacetonate	Modified Sol-gel synthesis	γ-Fe_2O_3 nanoparticles	8.5	23	74	Magnetic Hyperthermia Applications	[74]
Wasted condensed milk 'Can"	Acid leaching precipitation	γ-Fe_2O_3 Nanoparticles	26.90 to 52.15	54.94	65.45	Recycling and reuse of environmental waste	This work

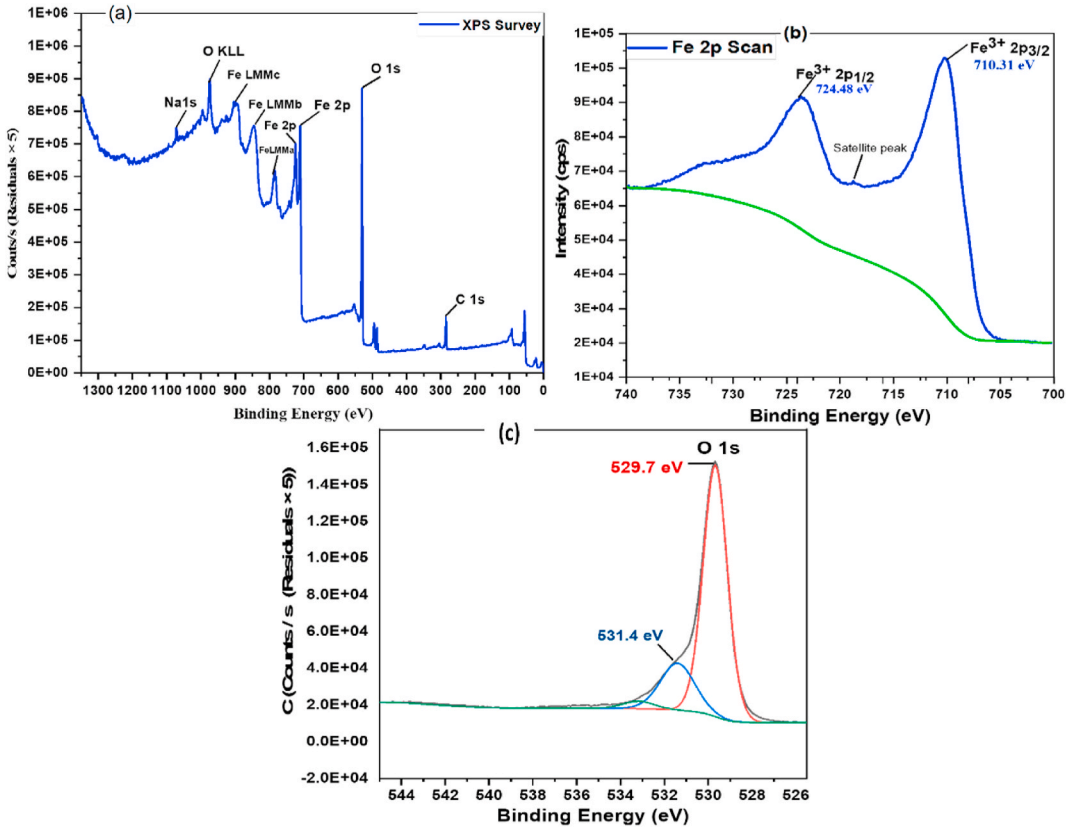

Fig. 10. XPS **(a)** survey spectrum of γ-Fe_2O_3 nanoparticles calcined at 350 °C, pH 14, **(b)** Fe narrow scan spectrum and **(c)** O narrow scan spectrum.

ferrimagnetic characteristics with high Ms (54.94 emu/g) and Hc (65.45 Oe). The findings contribute to the understanding that pH and calcination temperature play a vital role in nanomaterial synthesis. Finally, it can be said that this economically feasible and easy technique will be a great resolution for the recycling process which can be scale up for large production as well as prospective implementation in photocatalysis, humidity sensing, biomedicine, environmental remediation and energy storage.

CRediT authorship contribution statement

Bristy Biswas: Writing – original draft, Visualization, Software, Methodology, Investigation, Formal analysis, Data curation. **Md. Lutfor Rahman:** Writing – review & editing, Visualization, Validation, Supervision, Resources, Project administration, Methodology, Investigation, Funding acquisition, Data curation, Conceptualization. **Md. Farid Ahmed:** Visualization, Validation, Data curation. **Nahid Sharmin:** Writing – review & editing, Supervision, Resources, Project administration, Funding acquisition.

Declaration of competing interest

The authors declare that they have no known competing financial interests or personal relationships that could have appeared to influence the work reported in this paper.

Acknowledgements

The authors are thankful to the Strengthening of Institute of Glass and Ceramic Research & Testing (IGCRT) project (SIGCRT) of BCSIR, Institute of Energy Research & Development (IERD), BCSIR, Dhaka, and Central Analytical Research Facility (CARF), BCSIR for providing technical supports. The authors also gratefully acknowledge the Authority of BCSIR for encouraging them to carry out the research work and for financial support.

References

[1] A. Biswas, A.K. Patra, S. Sarkar, D. Das, D. Chattopadhyay, S. De, Synthesis of highly magnetic iron oxide nanomaterials from waste iron by one-step approach, Colloids Surfaces A Physicochem. Eng. Asp. 589 (2020) 124420, https://doi.org/10.1016/j.colsurfa.2020.124420.

[2] P. Samaddar, Y.S. Ok, K.H. Kim, E.E. Kwon, D.C.W. Tsang, Synthesis of nanomaterials from various wastes and their new age applications, J. Clean. Prod. 197 (2018) 1190–1209, https://doi.org/10.1016/j.jclepro.2018.06.262.

[3] H. Majeed, T. Iftikhar, K. Ahmad, K. Qureshi, Tabinda, F. Altaf, A. Iqbal, S. Ahmad, A. Khalid, Bulk industrial production of sustainable cellulosic printing fabric using agricultural waste to reduce the impact of climate change, Int. J. Biol. Macromol. 253 (2023) 126885, https://doi.org/10.1016/j.ijbiomac.2023.126885.

[4] B. Martínez, A. Roig, X. Obradors, E. Molins, A. Rouanet, C. Monty, Magnetic properties of γ-Fe2O3 nanoparticles obtained by vaporization condensation in a solar furnace, J. Appl. Phys. 79 (1996) 2580–2586, https://doi.org/10.1063/1.361125.

[5] M. V Kovalenko, M.I. Bodnarchuk, R.T. Lechner, F. Schäffler, W. Heiss, Supporting information for Fatty acid salts as Stabilizers in size- and shape-controlled nanocrystal synthesis : the case of iron oxide experimental details, J. Am. Chem. Soc. (2007) 1–12.

[6] L. Qiao, Z. Fu, J. Li, J. Ghosen, M. Zeng, J. Stebbins, P.N. Prasad, M.T. Swihart, Standardizing size- and shape-controlled synthesis of monodisperse magnetite (Fe3O4) nanocrystals by identifying and exploiting effects of organic impurities, ACS Nano 11 (2017) 6370–6381, https://doi.org/10.1021/acsnano.7b02752.

[7] C. Pascal, J.L. Pascal, F. Favier, M.L. Elidrissi Moubtassim, C. Payen, Electrochemical synthesis for the control of γ-Fe 2 O 3 nanoparticle size. Morphology, microstructure, and magnetic behavior, Chem. Mater. 11 (1999) 141–147, https://doi.org/10.1021/cm980742f.

[8] M. Coduri, P. Masala, L. Del Bianco, F. Spizzo, D. Ceresoli, C. Castellano, S. Cappelli, C. Oliva, S. Checchia, M. Allieta, D.V. Szabo, S. Schlabach, M. Hagelstein, C. Ferrero, M. Scavini, Local structure and magnetism of Fe2O3 maghemite nanocrystals: the role of crystal dimension, Nanomaterials 10 (2020), https://doi.org/10.3390/nano10050867.

[9] F.E. Osterloh, Inorganic materials as catalysts for photochemical splitting of water, Chem. Mater. 20 (2008) 35–54, https://doi.org/10.1021/cm7024203.

[10] J. Hu, G. Chen, I.M.C. Lo, Selective removal of heavy metals from industrial wastewater using maghemite nanoparticle: performance and mechanisms, J. Environ. Eng. 132 (2006) 709–715, https://doi.org/10.1061/(asce)0733-9372(2006)132:7(709).

[11] K.P. McKenna, F. Hofer, D. Gilks, V.K. Lazarov, C. Chen, Z. Wang, Y. Ikuhara, Atomic-scale structure and properties of highly stable antiphase boundary defects in Fe3O4, Nat. Commun. 5 (2014) 1–8, https://doi.org/10.1038/ncomms6740.

[12] S. Laurent, D. Forge, M. Port, A. Roch, C. Robic, L. Vander Elst, R.N. Muller, Magnetic iron oxide nanoparticles: synthesis, stabilization, vectorization, physicochemical characterizations and biological applications, Chem. Rev. 108 (2008) 2064–2110, https://doi.org/10.1021/cr068445e.

[13] W. Wu, Z. Wu, T. Yu, C. Jiang, W.S. Kim, Recent progress on magnetic iron oxide nanoparticles: synthesis, surface functional strategies and biomedical applications, Sci. Technol. Adv. Mater. 16 (2015) 23501, https://doi.org/10.1088/1468-6996/16/2/023501.

[14] Y. Trushkina, C.W. Tai, G. Salazar-Alvarez, Fabrication of maghemite nanoparticles with high surface area, Nanomaterials 9 (2019), https://doi.org/10.3390/nano9071004.

[15] Y. Cudennec, A. Lecerf, Topotactic transformations of goethite and lepidocrocite into hematite and maghemite, Solid State Sci. 7 (2005) 520–529, https://doi.org/10.1016/j.solidstatesciences.2005.02.002.

[16] A. Agarwal, H. Joshi, A. Kumar, Synthesis, characterization and application of nano lepidocrocite and magnetite in the degradation of carbon tetrachloride, South African, J. Chem. 64 (2011) 218–224.

[17] P. Xu, G.M. Zeng, D.L. Huang, C.L. Feng, S. Hu, M.H. Zhao, C. Lai, Z. Wei, C. Huang, G.X. Xie, Z.F. Liu, Use of iron oxide nanomaterials in wastewater treatment: a review, Sci. Total Environ. 424 (2012) 1–10, https://doi.org/10.1016/j.scitotenv.2012.02.023.

[18] T. Hyeon, Chemical synthesis of magnetic nanoparticles, Chem. Commun. 3 (2003) 927–934, https://doi.org/10.1039/b207789b.

[19] V. Arora, A. Sood, J. Shah, R.K. Kotnala, T.K. Jain, Synthesis and characterization of pectin-6-aminohexanoic acid-magnetite nanoparticles for drug delivery, Mater. Sci. Eng. C 80 (2017) 243–251, https://doi.org/10.1016/j.msec.2017.05.097.

[20] J. Dietrich, A. Enke, N. Wilharm, R. Konieczny, A. Lotnyk, A. Anders, S.G. Mayr, Energetic electron-assisted synthesis of tailored magnetite (Fe3O4) and maghemite (γ−Fe2O3) nanoparticles: structure and magnetic properties, Nanomaterials 13 (2023), https://doi.org/10.3390/nano13050786.

[21] R. Hachani, M.A. Birchall, M.W. Lowdell, G. Kasparis, L.D. Tung, B.B. Manshian, S.J. Soenen, W. Gsell, U. Himmelreich, C.A. Gharagouzloo, S. Sridhar, N.T. K. Thanh, Assessing cell-nanoparticle interactions by high content imaging of biocompatible iron oxide nanoparticles as potential contrast agents for magnetic resonance imaging, Sci. Rep. 7 (2017) 1–14, https://doi.org/10.1038/s41598-017-08092-w.

[22] S. Mornet, S. Vasseur, F. Grasset, P. Veverka, G. Goglio, A. Demourgues, J. Portier, E. Pollert, E. Duguet, Magnetic nanoparticle design for medical applications, Prog. Solid State Chem. 34 (2006) 237–247, https://doi.org/10.1016/j.progsolidstchem.2005.11.010.

[23] Z. Li, L. Wei, M. Gao, H. Lei, One-pot reaction to synthesize biocompatible magnetite nanoparticles, Adv. Mater. 17 (2005) 1001–1005, https://doi.org/10.1002/adma.200401545.

[24] M.F. Horst, D.F. Coral, M.B. Fernández van Raap, M. Alvarez, V. Lassalle, Hybrid nanomaterials based on gum Arabic and magnetite for hyperthermia treatments, Mater. Sci. Eng. C 74 (2017) 443–450, https://doi.org/10.1016/j.msec.2016.12.035.

[25] R.V. Morris, D.C. Golden, T.D. Shelfer, H.V. Lauer, Lepidocrocite to maghemite to hematite: a pathway to magnetic and hematitic Martian soil, Meteorit. Planet. Sci. 33 (1998) 743–751, https://doi.org/10.1111/j.1945-5100.1998.tb01680.x.

[26] J. Mähler, I. Persson, Rapid adsorption of arsenic from aqueous solution by ferrihydrite-coated sand and granular ferric hydroxide, Appl. Geochem. 37 (2013) 179–189, https://doi.org/10.1016/j.apgeochem.2013.07.025.

[27] P.L. Taberna, S. Mitra, P. Poizot, P. Simon, J.M. Tarascon, High rate capabilities Fe3O4-based Cu nano-architectured electrodes for lithium-ion battery applications, Nat. Mater. 5 (2006) 567–573, https://doi.org/10.1038/nmat1672.

[28] L. Wei, M.C. Wu, T.S. Zhao, Y.K. Zeng, Y.X. Ren, An aqueous alkaline battery consisting of inexpensive all-iron redox chemistries for large-scale energy storage, Appl. Energy 215 (2018) 98–105, https://doi.org/10.1016/j.apenergy.2018.01.080.

[29] J. Chen, L. Xu, W. Li, X. Gou, α-Fe2O3 nanotubes in gas sensor and lithium-ion battery applications, Adv. Mater. 17 (2005) 582–586, https://doi.org/10.1002/adma.200401101.

[30] M. Valvo, F. Lindgren, U. Lafont, F. Björefors, K. Edström, Towards more sustainable negative electrodes in Na-ion batteries via nanostructured iron oxide, J. Power Sources 245 (2014) 967–978, https://doi.org/10.1016/j.jpowsour.2013.06.159.

[31] B. Koo, H. Xiong, M.D. Slater, V.B. Prakapenka, M. Balasubramanian, P. Podsiadlo, C.S. Johnson, T. Rajh, E.V. Shevchenko, Hollow iron oxide nanoparticles for application in lithium ion batteries, Nano Lett. 12 (2012) 2429–2435, https://doi.org/10.1021/nl3004286.

[32] Y.F. Shen, J. Tang, Z.H. Nie, Y.D. Wang, Y. Ren, L. Zuo, Tailoring size and structural distortion of Fe3O4 nanoparticles for the purification of contaminated water, Bioresour. Technol. 100 (2009) 4139–4146, https://doi.org/10.1016/j.biortech.2009.04.004.

[33] E. Roduner, Size matters: why nanomaterials are different, Chem. Soc. Rev. 35 (2006) 583–592, https://doi.org/10.1039/b502142c.

[34] C. Burda, X. Chen, R. Narayanan, M.A. El-Sayed, Chemistry and properties of nanocrystals of different shapes. https://doi.org/10.1002/chin.200527215, 2005.

[35] D. Cao, H. Li, L. Pan, J. Li, X. Wang, P. Jing, X. Cheng, W. Wang, J. Wang, Q. Liu, High saturation magnetization of γ 3-Fe2 O3 nano-particles by a facile one-step synthesis approach, Sci. Rep. 6 (2016) 1–9, https://doi.org/10.1038/srep32360.

[36] O. Bomati Miguel, M.P. Morales, C.J. Serna, S. Veintemillas-Verdaguer, Magnetic nanoparticles prepared by laser pyrolysis, IEEE Trans. Magn. 38 (2002) 2616–2618, https://doi.org/10.1109/TMAG.2002.801961.

[37] M.J. Tueros, L.A. Baum, R.A. Borzi, S.J. Stewart, R.C. Mercader, S.G. Marchetti, J.F. Bengoa, L.V. Mogni, Characterization of nanosized maghemite particles prepared by microemulsion using an ionic surfactant, Hyperfine Interact. 148–149 (2003) 103–108, https://doi.org/10.1023/B:HYPE.0000003770.22742.e7.

[38] R.S. Sapieszko, E. Matijevic, Preparation of well defined colloidal particles by thermal decomposition of metal chelates - 2. Cobalt and nickel, Corrosion 36 (1980) 522–530, https://doi.org/10.5006/0010-9312-36.10.522.

[39] S. Layek, A. Pandey, A. Pandey, H. Verma, Synthesis of γ–Fe2O3 nanoparticles with crystallographic and magnetic texture, Int. J. Eng. Sci. Technol. 2 (2011) 33–39, https://doi.org/10.4314/ijest.v2i8.63778.

[40] Z. Li, H. Chen, H. Bao, M. Gao, One-Pot reaction to synthesize water-soluble magnetite nanocrystals, Chem. Mater. 16 (2004) 1391–1393, https://doi.org/10.1021/cm035346y.

[41] K.M. Rahman, B. Biswas, T. Neger, N. Sharmin, L. Rahman, Method validation on iron determination by spectrophotometric method in aqueous medium, Indian J. Chem. 59 (2020) 790–796.

[42] R.A. Judge, R.S. Jacobs, T. Frazier, E.H. Snell, M.L. Pusey, The effect of temperature and solution pH on the nucleation of tetragonal lysozyme crystals, Biophys. J. 77 (1999) 1585–1593, https://doi.org/10.1016/S0006-3495(99)77006-2.

[43] S.K. Sen, U.C. Barman, M.S. Manir, P. Mondal, X-ray peak profile analysis of pure and Dy-doped α -MoO 3 nanobelts using Halder-Wagner methods, Adv. Nat. Sci. Nanosci. Nanotechnol. 11 (2020).

[44] A.R. Stokes, A.J. C Wilson, P. Mag, B.A. R Stokes, A.J. Wilson, J. Am. Chem. Soc. 57 (1935) 150, 1928. 2. Phys. 49, 428 ; 1930 a.

[45] V. Mote, Y. Purushotham, B. Dole, Williamson-Hall analysis in estimation of lattice strain in nanometer-sized ZnO particles, J. Theor. Appl. Phys. 6 (2012) 2–9, https://doi.org/10.1186/2251-7235-6-6.

[46] S.K. Sen, T.C. Paul, S. Dutta, M.N. Hossain, M.N.H. Mia, XRD peak profile and optical properties analysis of Ag-doped h-MoO3 nanorods synthesized via hydrothermal method, J. Mater. Sci. Mater. Electron. 31 (2020) 1768–1786, https://doi.org/10.1007/s10854-019-02694-y.

[47] M. Basak, M.L. Rahman, M.F. Ahmed, B. Biswas, N. Sharmin, The use of X-ray diffraction peak profile analysis to determine the structural parameters of cobalt ferrite nanoparticles using Debye-Scherrer, Williamson-Hall, Halder-Wagner and Size-strain plot: different precipitating agent approach, J. Alloys Compd. 895 (2022) 162694, https://doi.org/10.1016/j.jallcom.2021.162694.

[48] H. Yadav, N. Sinha, S. Goel, B. Kumar, Eu-doped ZnO nanoparticles for dielectric, ferroelectric and piezoelectric applications, J. Alloys Compd. 689 (2016) 333–341, https://doi.org/10.1016/j.jallcom.2016.07.329.

[49] M.K. Hossain, A.A. Mortuza, S.K. Sen, M.K. Basher, M.W. Ashraf, S. Tayyaba, M.N.H. Mia, M.J. Uddin, A comparative study on the influence of pure anatase and Degussa-P25 TiO2 nanomaterials on the structural and optical properties of dye sensitized solar cell (DSSC) photoanode, Optik 171 (2018) 507–516, https://doi.org/10.1016/j.ijleo.2018.05.032.

[50] M. Basak, M.L. Rahman, M.F. Ahmed, B. Biswas, N. Sharmin, Calcination effect on structural, morphological and magnetic properties of nano-sized CoFe2O4 developed by a simple co-precipitation technique, Mater. Chem. Phys. 264 (2021), https://doi.org/10.1016/j.matchemphys.2021.124442.

[51] N.K. Das, J. Chakrabartty, S.F.U. Farhad, A.K. Sen Gupta, E.M.K. Ikball Ahamed, K.S. Rahman, A. Wafi, A.A. Alkahtani, M.A. Matin, N. Amin, Effect of substrate temperature on the properties of RF sputtered CdS thin films for solar cell applications, Results Phys. 17 (2020), https://doi.org/10.1016/j.rinp.2020.103132, 0–7.

[52] V. Madhavi, T.N.V.K.V. Prasad, A.V.B. Reddy, B. Ravindra Reddy, G. Madhavi, Application of phytogenic zerovalent iron nanoparticles in the adsorption of hexavalent chromium, Spectrochim. Acta Part A Mol. Biomol. Spectrosc. 116 (2013) 17–25, https://doi.org/10.1016/j.saa.2013.06.045.

[53] I. de la Calle, D. Soto-Gómez, P. Pérez-Rodríguez, J.E. López-Periago, Particle size characterization of sepia ink eumelanin biopolymers by SEM, DLS, and AF4-MALLS: a comparative study, Food Anal. Methods 12 (2019) 1140–1151, https://doi.org/10.1007/s12161-019-01448-0.

[54] S. Islam, M. Lutfor Rahman, M. Rassel Moni, B. Biswas, M. Farid Ahmed, N. Sharmin, Impacts of annealing temperature on microstructure, optical and electromagnetic properties of zinc ferrites nanoparticles synthesized by polymer assisted sol-gel method, Arab. J. Chem. 16 (2023) 105186, https://doi.org/10.1016/j.arabjc.2023.105186.

[55] A. Bootz, V. Vogel, D. Schubert, J. Kreuter, Comparison of scanning electron microscopy, dynamic light scattering and analytical ultracentrifugation for the sizing of poly(butyl cyanoacrylate) nanoparticles, Eur. J. Pharm. Biopharm. 57 (2004) 369–375, https://doi.org/10.1016/S0939-6411(03)00193-0.

[56] A. Begum, A. Hussain, A. Rahman, Effect of deposition temperature on the structural and optical properties of chemically prepared nanocrystalline lead selenide thin films, Beilstein J. Nanotechnol. 3 (2012) 438–443, https://doi.org/10.3762/bjnano.3.50.

[57] R. Prabhakar, S.R. Samadder, Low cost and easy synthesis of aluminium oxide nanoparticles for arsenite removal from groundwater: a complete batch study, J. Mol. Liq. 250 (2018) 192–201, https://doi.org/10.1016/j.molliq.2017.11.173.

[58] M. Jafarpour, M. Rostami, S. Khalkhali, H. Nikmanesh, M. Ara, The effect of lanthanum substitution on the structural, magnetic, and dielectric properties of nanocrystalline Mn-Ni spinel ferrite for radio frequency (RF) applications, Phys. Lett. 446 (2022) 128285, https://doi.org/10.1016/j.physleta.2022.128285.

[59] M. Bloemen, W. Brullot, T.T. Luong, N. Geukens, A. Gils, T. Verbiest, Improved functionalization of oleic acid-coated iron oxide nanoparticles for biomedical applications, J. Nanoparticle Res. 14 (2012), https://doi.org/10.1007/s11051-012-1100-5.

[60] F. Majid, A. Nazir, S. Ata, I. Bibi, H.S. Mehmood, A. Malik, A. Ali, M. Iqbal, Effect of hydrothermal reaction time on electrical, structural and magnetic properties of cobalt ferrite, Zeitschrift Fur Phys. Chemie 234 (2020) 323–353, https://doi.org/10.1515/zpch-2019-1423.

[61] J. Larsson, M. Hill, A. Duffy, J. Suspension staDuffy, A. Hill, 2011, Suspension Stability : Why Particle Size , Zeta Potential and Rheology Are Important, vol. 20, 2011, pp. 1–35. Malvern.Com, 20, 1–35.bility : Why particle size , zeta potential and rheology are important, Www.Malvern.Com.

[62] C. Freitas, R.H. Müller, Effect of light and temperature on zeta potential and physical stability in solid lipid nanoparticle (SLN®) dispersions, Int. J. Pharm. 168 (1998) 221–229, https://doi.org/10.1016/S0378-5173(98)00092-1.

[63] R. Grau-Crespo, A.Y. Al-Baitai, I. Saadoune, N.H. De Leeuw, Vacancy ordering and electronic structure of γ-Fe2O 3 (maghemite): a theoretical investigation, J. Phys. Condens. Matter 22 (2010) 1–19, https://doi.org/10.1088/0953-8984/22/25/255401.

[64] J. Wallyn, N. Anton, T.F. Vandamme, Synthesis, principles, and properties of magnetite nanoparticles for in vivo imaging applications—a review, Pharmaceutics 11 (2019) 1–29, https://doi.org/10.3390/pharmaceutics11110601.

[65] Y. Liu, J. Hsu, The use of co-precipitation to produce Nano-Mn-Zn Ferrite ([MnxZn1-x]Fe2O4) from waste batteries, Appl. Sci. 8 (2018), https://doi.org/10.3390/app8061005.

[66] Y. Hadadian, H. Masoomi, A. Dinari, C. Ryu, S. Hwang, S. Kim, B.K. Cho, J.Y. Lee, J. Yoon, From low to high saturation magnetization in magnetite nanoparticles: the crucial role of the molar ratios between the chemicals, ACS Omega (2022), https://doi.org/10.1021/acsomega.2c01136.

[67] M.A. Almessiere, Y. Slimani, A. Demir Korkmaz, S. Güner, A. Baykal, S.E. Shirsath, I. Ercan, P. Kögerler, Sonochemical synthesis of Dy3+ substituted Mn0.5Zn0.5Fe2−xO4 nanoparticles: structural, magnetic and optical characterizations, Ultrason. Sonochem. 61 (2020) 104836, https://doi.org/10.1016/j.ultsonch.2019.104836.

[68] R. Singh Yadav, I. Kuřitka, J. Vilcakova, T. Jamatia, M. Machovsky, D. Skoda, P. Urbánek, M. Masař, M. Urbánek, L. Kalina, J. Havlica, Impact of sonochemical synthesis condition on the structural and physical properties of MnFe2O4 spinel ferrite nanoparticles, Ultrason. Sonochem. 61 (2020) 104839, https://doi.org/10.1016/j.ultsonch.2019.104839.

[69] M. Kouser, B. Chowhan, N. Sharma, M. Gupta, Transformation of waste toner powder into valuable Fe2O3Nanoparticles for the preparation of recyclable Co(II)-NH2-SiO2@Fe2O3 and its applications in the synthesis of polyhydroquinoline and quinazoline derivatives, ACS Omega 7 (2022) 47619–47633, https://doi.org/10.1021/acsomega.2c04512.

[70] Z. Cheng, A.L.K. Tan, Y. Tao, D. Shan, K.E. Ting, X.J. Yin, Synthesis and characterization of iron oxide nanoparticles and applications in the removal of heavy metals from industrial wastewater, Int. J. Photoenergy 2012 (2012), https://doi.org/10.1155/2012/608298.

[71] T.A. Aragaw, B.A. Aragaw, Synthesis and characterization of α-Fe2O3/γ-Fe2O3-nanoparticles from recyclable electro-coagulated sludge: insights and predictions for different application, SN Appl. Sci. 2 (2020) 1–12, https://doi.org/10.1007/s42452-020-03553-w.

[72] V. Kumar, A. Barala, V.K. Goel, Synthesis of iron oxide nanoparticles from scrapped waste materials for efficient dye removal to purify industrial waste water, Indian J, Pure Appl. Phys. 61 (2023) 903–905, https://doi.org/10.56042/ijpap.v61i11.3113.

[73] G. Ren, X. Wang, Z. Zhang, B. Zhong, L. Yang, D. Xu, X. Yang, Facile synthesis of maghemite nanoparticle from waste green vitriol as adsorbent for adsorption of arsenite, J. Mol. Liq. 259 (2018) 32–39, https://doi.org/10.1016/j.molliq.2018.02.132.

[74] O.M. Lemine, N. Madkhali, M. Alshammari, S. Algessair, A. Gismelseed, L. El Mir, M. Hjiri, A.A. Yousif, K. El-boubbou, Maghemite (γ-fe2o3) and γ-fe2o3-tio2 nanoparticles for magnetic hyperthermia applications: synthesis, characterization and heating efficiency, Materials 14 (2021) 1–18, https://doi.org/10.3390/ma14195691.

[75] T. Shahjuee, S. Morteza Masoudpanah, S. Mohammad Mirkazemi, Coprecipitation synthesis of CoFe2O4 nanoparticles for hyperthermia, J. Ultrafine Grained Nanostruct. Mater. 50 (2017) 105–110, https://doi.org/10.22059/JUFGNSM.2017.02.04.

[76] Y. Zhang, L. Li, W. Ma, Y. Zhang, M. Yu, J. Guo, H. Lu, C. Wang, Two-in-one strategy for effective enrichment of phosphopeptides using magnetic mesoporous γ-Fe2O3 nanocrystal clusters, ACS Appl. Mater. Interfaces 5 (2013) 614–621, https://doi.org/10.1021/am3019806.

[77] T. Fujii, F.M.F. de Groot, G.A. Sawatzky, F.C. Voogt, T. Hibma, K. Okada, In situ xps analysis of various iron oxide films grown by (formula presented)-assisted molecular-beam epitaxy, Phys. Rev. B Condens. Matter 59 (1999) 3195–3202, https://doi.org/10.1103/PhysRevB.59.3195.

[78] H. Kong, J. Song, J. Jang, One-step fabrication of magnetic γ-Fe2O 3/polyrhodanine nanoparticles using in situ chemical oxidation polymerization and their antibacterial properties, Chem. Commun. 46 (2010) 6735–6737, https://doi.org/10.1039/c0cc00736f.
[79] M.V. Nikolic, Z.Z. Vasiljevic, M.D. Lukovic, V.P. Pavlovic, J.B. Krstic, J. Vujancevic, N. Tadic, B. Vlahovic, V.B. Pavlovic, Investigation of ZnFe 2 O 4 spinel ferrite nanocrystalline screen-printed thick films for application in humidity sensing, Int. J. Appl. Ceram. Technol. 16 (2019) 981–993, https://doi.org/10.1111/ijac.13190.
[80] S. Das, M.L. Rahman, P.P. Mondal, P.L. Mahapatra, D. Saha, Screen-printed MgAl2O4 semi-thick film based highly sensitive and stable capacitive humidity sensor, Ceram. Int. 47 (2021) 33515–33524, https://doi.org/10.1016/j.ceramint.2021.08.260.